Communication-Based Control for DC Microgrids

Mahmoud Saleh[©], Student Member, IEEE, Yusef Esa, Student Member, IEEE, and Ahmed A. Mohamed , Senior Member, IEEE

Abstract-Centralized communication-based control is one of the main methods that can be implemented to achieve autonomous advanced energy management capabilities in dc microgrids. However, its major limitation is the fact that communication bandwidth and computation resources are limited in practical applications. This can be often improved by avoiding redundant communications and complex computations. In this paper, an autonomous communication-based hybrid state/event driven control scheme is proposed. This control scheme is hierarchical and heuristic, such that on the primary control level, it encompasses state-driven local controllers, and on the secondary control level, an event-driven microgrid centralized controller is used. This heuristic hybrid control system aims at reducing the communication load and complexity, processor computations, and consequently system cost while maintaining reliable autonomous operation during all possible scenarios. A mathematical model for the proposed control scheme using finite state machines has been developed and used to cover all the possible modes/sub-modes of operation, and assure seamless transitions among them during various events. Results of some case studies involving severe operational scenarios were presented and discussed. Results verify the validity and effectiveness of the proposed communication-based control

Index Terms—Communication-based control, DC microgrids, finite state machine, hybrid state/event driven control.

Nomenclature

DC/DC Bidirectional Converter

$G_{ch}(S)$	Charging current controller transfer function.
$G_{dch}(S)$	Discharging current controller transfer func-
	tion.
$G_{v}^{bi}(S) _{ol}$ $G_{i}^{bi}(S)$	Outer loop voltage controller transfer function.
$G_i^{bi}(S)$	Current controller general transfer function
•	with FSM.
$G_T^{bi}(S)$	Bidirectional converter local controller (LC _{Bi})
-	general transfer function with FSM.

 $G_{\nu}^{bi}(S)$ Voltage controller general transfer function with FSM.

Manuscript received March 8, 2017; revised July 2, 2017 and October 13, 2017; accepted November 26, 2017. Date of publication January 8, 2018; date of current version February 18, 2019. Paper no. TSG-00338-2017. (Corresponding author: Ahmed A. Mohamed.)

M. Saleh and Y. Esa are with the Smart Grid Laboratory, Department of Electrical Engineering, City University of New York, New York, NY 10031 USA (e-mail: mahmoudsah@hotmail.com; yusefesa@gmail.com).

A. A. Mohamed is with the Smart Grid Laboratory, Department of Electrical Engineering, City University of New York, New York, NY 10031 USA, on leave from the Department of Electrical Engineering, Menia University, Menia 61519, Egypt (e-mail: amohamed@ccny.cuny.edu).

Color versions of one or more of the figures in this paper are available online at http://ieeexplore.ieee.org.

Digital Object Identifier 10.1109/TSG.2018.2791361

I_{l}^{ref}	Charging current reference.
$I_{ch}^{ref} \ I_{ch}^* \ I_{ch}^{ref} \ I_{dch}^{ref}$	Battery measured charging current.
I_{i}^{ref}	Discharging current reference.
I_{dch}^*	Measured discharging current on the DC
	bus side.
I_{in}^{bi}	Input current from the battery system.
$I_{in}^{bi} \ I_{out}^{bi}$	Output current to the DC bus.
I_{ref}	Reference for current control.
I_{1c}	Battery system rated current at 1C rate of
	charge /discharge.
K_{p1}^{i}, K_{i1}^{i} K_{p2}^{i}, K_{i2}^{i} K_{p3}^{v}, K_{i3}^{v} K_{p4}^{v}, K_{i4}^{v}	Proportional and integral gains of the $G_{ch}(S)$.
K_{n2}^{i}, K_{i2}^{i}	Proportional and integral gains of the $G_{dch}(S)$.
K_{n3}^{v}, K_{i3}^{v}	Proportional and integral gains of the $G_v^{bi}(S) _{ol}$.
K_{n4}^{v}, K_{i4}^{v}	Proportional and integral gains of the charging
P	inner loop of $G_i^{bi}(S)$.
K_{p5}^{v}, K_{i5}^{v}	Proportional and integral gains of the discharg-
•	ing inner loop of $G_i^{bi}(S)$.
$P_{v}^{bi}(m)$	A function representing the summation of the
,	sub-modes, which enable voltage control in
	$G_T^{bi}(S)$.
$P_{i1}^{bi}(m)$	A function representing the summation of the
*1	sub-modes, which enable charging current con-
	trol in $G_T^{bi}(S)$.
$P_{i2}^{bi}(m)$	A function representing the summation of the
14	

sub-modes, which enable discharging current

Bidirectional converter solid state relay.

control in $G_T^{bi}(S)$.

Output voltage.

DC bus reference voltage. DC bus measured voltage.

D0

 SSR_{Bi}

C/DC Boost	Converter
$G_T^{bo}(S)$	Boost converter local controller (LC_{Bo}) general transfer function with FSM.
$G_{v}^{bo}(S)$	Voltage control transfer function.
K_{p6}^{v}, K_{i6}^{v}	Proportional and integral gains of $G_v^{bo}(S)$.
MPPT(S)	Maximum power point tracking algorithm
	transfer function.
$P_i^{bo}(m)$	A function representing the summation of the
	sub-modes, which enable MPPT in $G_T^{bo}(S)$.
$P_{v}^{bo}(m)$	A function representing the summation of the
	sub-modes, which enable voltage control in
	$G_T^{bo}(S)$.
SSR_{Bo}	Boost converter solid state relay.
V_{-}^{bo}	Boost converter output voltage.

DC/AC Inverter

D C/11C 1/1/C/1	
$G_{ac}^{inv}(S)$	AC voltage control transfer function with FSM.
$G_{DC}^{inv}(S) _{ol}$	Outer loop DC voltage control transfer function
	with FSM.
$G_{DC}^{inv}(S)$	DC voltage control transfer function with FSM.
$G_{id}^{inv}(S)$	d-axis current control transfer function.
$G_{iq}^{inv}(S)$	q-axis current control transfer function with
ž	FSM in the $dq0$ -frame of references.
$G_T^{inv}(S)$	Inverter local controller(LC _{Inv}) general transfer
	function with FSM.
$I_d^* \ I_d^{ref}$	<i>d</i> -axis component of the measured AC current.
I_d^{rej}	d-axis reference current for the active current
	controller.
$I_q^* \ I_q^{ref}$	<i>q</i> -axis component of the measured AC current.
I_q^{ref}	q-axis reference current for the reactive current
	controller.
K_{p7}^{ac}, K_{i7}^{ac}	Proportional and integral gains of $G_{ac}^{inv}(S)$.
K_{n8}^{DC}, K_{i8}^{DC}	Proportional and integral gains of $G_{DC}^{inv}(S) _{ol}$.
K_{p9}^{DC} , K_{i9}^{DC}	Proportional and integral gains of $G_{DC}^{inv}(S)$.
$K_{p10}^{id}, K_{i10}^{id}$	Proportional and integral gains of $G_{id}^{inv}(S)$.
$K_{p11}^{iq}, K_{i11}^{iq}$	Proportional and integral gains of $G_{iq}^{inv}(S)$.
$P_{ac}^{inv}(m)$	A function representing the summation of the
	sub-modes, which enable AC voltage control in
	$G_T^{inv}(S)$.
$P_{DC}^{inv}(m)$	A function representing the summation of the
	sub-modes, which enable DC voltage control in
-im	$G_T^{inv}(S)$.
$P_i^{inv}(m)$	A function representing the summation of the
	sub-modes, which enable charging current con-
GGD	trol of $G_{id}^{inv}(S)$ and/or $G_{iq}^{inv}(S)$ in $G_T^{inv}(S)$.
SSR_{Grid}	Solid state relay connecting the grid to the
	DC MG.

FSM Transition Variables

 $SSR_{Inv} \\$

 V^{ph}

 V_{ph}^{ref}

 t_s

B_{od}	LC _{Bi} signal representing whether the battery is
	being over discharged or not.
\mathcal{C}_U	Signal triggering utility control.
\mathcal{E}_P	Alarm signal representing whether the energy
	price is high or low.
\mathcal{R}_{inv}	Solid state relay signal within the inverter zone.
\mathcal{R}_{Grid}	Solid state relay signal within the PCC zone.
\mathcal{R}_{Bi}	Solid state relay signal within the bidirectional
	converter zone.
\mathcal{R}_{Bo}	Solid state relay signal within the boost con-
	verter zone.
S_{AC}	AC agent signal reporting violations of AC bus
	operational limits.
S_{DC}	DC agent signal reporting violations of DC bus
	operational limits.
SOC	Battery system state of charge signaled by the

Settling time of converters PI controllers.

Inverter solid state relay.

AC bus reference RMS phase voltage.

AC bus measured RMS phase voltage.

Load Shedding

$LS_{AC} _1$	First level of AC load shedding.
$LS_{AC} _2$	Second level of AC load shedding.
$LS_{DC} _1$	First level of DC load shedding.
$LS_{DC} _2$	Second level of DC load shedding.
$LS_T _1$	First level of total load shedding.
$LS_T _2$	Second level of total load shedding.
$LS_T _3$	Third level of total load shedding.
$LS_T _4$	Fourth level of total load shedding.
P_b	Battery system available power.
P_{ch}	Battery system charging power.
$P_{DCn}^{LS}(m)$	A function representing the summation of sub-
Den	modes, which trigger $LS_{DC} _n$, where $n = 1, 2, 3$
	and 4.
P_D	Load demand power.
P_m	Safety reserve to account for solar intermit-
	tency.
$P_{pv} _{Lst2}$	Solar system available power at the moment of
•	executing $LS_T _2$.
$P_{pv} _{Lst4}$	Solar system available peak power within an
•	hour interval right before executing $LS_T _4$.
$P_{Res} _{Lst1}$	Available DC MG resources at the moment of
	executing $LS_T _1$.
$P_{DCn}^{LS}(m)$	A function representing the summation of sub-
2011	modes, which trigger $LS_{DC} _n$, where $n = 1, 2, 3$

I. Introduction

and 4.

ICROGRID is a key foundational building block of future smart grids. It has the potential to prominently increase the grid resiliency in the face of natural disasters [1]–[3]. A microgrid -according to the definitions adopted by the U.S. Department of Energy and some European agencies- refers to a group of interconnected loads, distributed energy resources (DERs), and energy storage systems (ESS), which acts as a single controllable entity with respect to the grid. Microgrids connect to the main grid through one or more nodes, namely the points of common coupling (PCC). Depending on the grid availability among other conditions, a microgrid must be able to operate in either grid-connected or islanded mode [4], [5].

A microgrid can be categorized based on the voltage of its common bus, which links the various resources and loads into AC, DC, or hybrid AC/DC. Compared to DC MGs, AC ones are known to be less efficient since more conversion stages are required to link DERs and ESS, which are mostly DC [6], [7].

In contrast, in DC microgrids, the common bus is DC. Advantageously, time synchronization among microgrid assets is not required and power factor losses are omitted. However, DC microgrids impose some challenges, especially related to the design of effective protection systems [8]–[10]. Hybrid AC/DC microgrids evolved to harness the benefits of both topologies, especially if AC and DC sources of energy are to be used. Nevertheless, they require relatively complex control schemes [11]–[14]. This paper is focused on DC microgrids.

DC microgrid control can be generally achieved using one of two approaches: (1) communication-based control; and (2) voltage-based droop control. The later approach is achieved by adding a virtual resistor to the converter's voltage regulator, which enables current/power sharing. Among some other advantages, first and foremost, voltage-based droop control enables achieving autonomous control without the need for a communication system [15]-[19]. In this control type, the various microgrid resources use the DC bus voltage to signal load/generation mismatches; therefore, it is analogous to frequency droop control in AC networks. Droop control enables power sharing while providing active damping to the system, and it offers a plug and play feature since new converters can be seamlessly integrated to the DC bus [20], [21]. However, droop control has some major drawbacks. For instance, circulating currents between connected converters may appear due to minor inaccuracies and uncertainties in voltage set points [22]. Besides, it has a slow dynamic response and can cause microgrid stability degradation [23]. Most importantly, it fails to achieve the optimal coordinated performance of the MG.

On the other hand, communication-based coordinated control, as the name implies, is based on continuous communication among the various microgrid resources. In this approach, microgrid control can be centralized, or fully distributed. In centralized communication-based control, all sensors' data (i.e., microgrid states) are transmitted from the local DERs controllers to a microgrid central controller (MGCC) in real time. The MGCC processes the data and sends back control actions, and operational set points to the local controllers. Since the MGCC has real-time information on all microgrid assets and loads, optimization algorithms can be used to reach optimal, or near-optimal, microgrid performance. However, communication-based control's reliability is mostly dependent on that of the communication system. Moreover, it is subject to single point failures.

In distributed communication-based control, no central controller is required, which relatively increases the reliability. Local controllers communicate directly and coordinate/negotiate to achieve microgrid optimal control. Distributed communication-based control is immune to single point failure; however, its main limitations include complexity of analytical performance analysis, e.g., evaluation of convergence speed and stability margins in a non-ideal system that contains communication time delays and measurement errors is challenging [24].

Communication-based control has received considerably less attention than droop control in the literature since there has been a consensus that dependence on communication networks would lead to compromised reliability. In addition, utilizing droop control for microgrids seems more convenient since it builds upon our experiences with controlling the main grid. With advances in communication technologies (e.g., the transition to 5G and Internet of Things), it is envisioned that the smart grid of the future will consist of a myriad of microgrids that continuously coordinate with each other and with the main grid. Therefore, increased reliance on communication will become inevitable. While the focus of this paper is on

the development, verification, and testing of communicationbased controllers, we studied other essential aspects related to power system/communication network interdependencies, such as the impact of communication latency on microgrids with communication-based control [25], [26].

The flow of data and commands within the microgrid can be designed to be either "state driven" or "event driven." In state-driven control, also called time-driven control, the control commands are determined based on the values of the system state variables, which must be continuously communicated with the central controller. The state variable signals of the system to be controlled (e.g., a microgrid converter voltage and current) are sampled at a constant rate and then transmitted periodically. In contrast, event-driven controllers are triggered by externally generated events, where clock/continuous measurements are not dictating actions; rather, events trigger actions or operating modes. Event signals are only transmitted when certain conditions change, which requires smaller communication bandwidth compared to that of the state driven control. Event driven control is of importance because of its better resource utilization. This is due to the fact that reducing the number of control updates leads directly to a reduction in the number of bits (i.e., signals) to be transmitted and thus to a lower average bus load and less computational processing. Moreover, lower communication bus loads and computational processing also save energy [27], [28]. However, it should be noted that event-driven control requires a deep understanding of the system understudy to increase the readiness level and avoid unexpected events that might lead to system debacle. Although the above discussion indicates that in smart grid applications (e.g., microgrid) it may seem logical to study and implement event-driven controllers, their implementation is scarce. One of the reasons that state driven control still dominates may be due to the difficulty involved in developing a system theory that fits event-driven systems in which the continuous dynamics are profound [27]. Conventional state driven controllers are designed with the main focus on the performance of the controlled process. Event driven control may be suitable for certain applications to balance between control performance and system efficiency.

Previous research on microgrid control either focused on a particular case [29] or did not consider all possible scenarios/modes of operation [15]–[19]. Moreover, it was mostly focused on the stability aspects, i.e., finding controller parameters that would guarantee stable performance [30]-[33]. Some researches were focused mainly on decentralized communication-based control that requires high processing capabilities at each local controller and includes considerable complexity of analytical performance [34], [35]. Other researchers tried to improve the droop control method by integrating it with a low-bandwidth communication decentralized control scheme, which solves some of the inherent problems of the droop control successfully [36]. Their proposed controller achieves autonomous operation but does not help reach near-optimal performance. It requires low but constant communication bandwidth. Also, the work was introduced for two converters only; however, as the number of converters increases the complexity increases. The work in [37] proposed

a novel approach to modify the conventional droop control (i.e., three level autonomous control scheme based on different voltage levels). However, the work did not discuss protection considerations regarding different voltage levels.

It was observed in the literature that event and state driven controls received minimal attention. In this paper, a novel hybrid state/event driven autonomous communication-based controller for DC microgrids will be developed. The proposed control architecture is hierarchical and heuristic, such that the primary control layer is state driven; whereas, the secondary control layer is event driven. This design aims at balancing between MG control performance and other objectives, such as reducing processing load, communication load and overall system cost. A finite state machine (FSM) has been used to realize the proposed controller including the event driven control. The developed controller mainly aims at guaranteeing the survivability/resiliency and reliability of the MG during all possible operational scenarios.

II. HIERATICAL HYBRID STATE/EVENT DRIVEN CONTROL

The topology of the DC microgrid under study in this paper is illustrated in Fig. 1. It consists of the followings: a 4.5 kW photovoltaic (PV) system connected to the DC bus through a DC/DC boost converter, a 1.4 kWh battery system integrated to the DC bus through a bidirectional DC/DC charger, a bidirectional AC/DC smart inverter tying the DC MG to the main grid. The voltage of the common DC bus in the MG is 300 V. It has a total load of 6 kW connected to the DC bus, and three-phase 2 kW connected to the AC bus. The values of all the converter parameters can be found in the Appendix, Table A.I. Further details about the design of this microgrid can be found in [2] and [38]. Two designs were studied, to show the impact of different designs on the control modes. In Design one (D1), a portion of the MG loads is connected to the AC bus, and another portion is connected to the DC bus, as shown in Fig. 1. In Design two (D2), the loads are all connected to the DC bus (these may include DC loads directly connected, or inverter-interfaced AC loads). This will further be demonstrated in Section III.

We will adopt a hierarchical control architecture as shown in Fig. 2. In the primary control layer, local controllers (LCs) of the various converters are state driven. Each LC continuously monitors some state variables that are required to maintain its assigned mode or operating point, as long as it has not received a new command from the secondary controller (i.e., the MGCC). DC and AC agents act as islanding relays whose functionality is to detect any violation, e.g., grid frequency drop, according to standards [39], [40]. Other relays within the MG protection system also report any fault to the MGCC.

In the secondary control layer, an MGCC communicates with the LCs, islanding agents and protection relays. The operating modes are assigned to each LC by the MGCC. The secondary control layer between the MGCC and the LCs, islanding agents and protection relays is event driven, i.e., it does not require continuous communication with the LCs. The devised heuristic logic within the MGCC was conceived such that it takes an instant action only if a new event

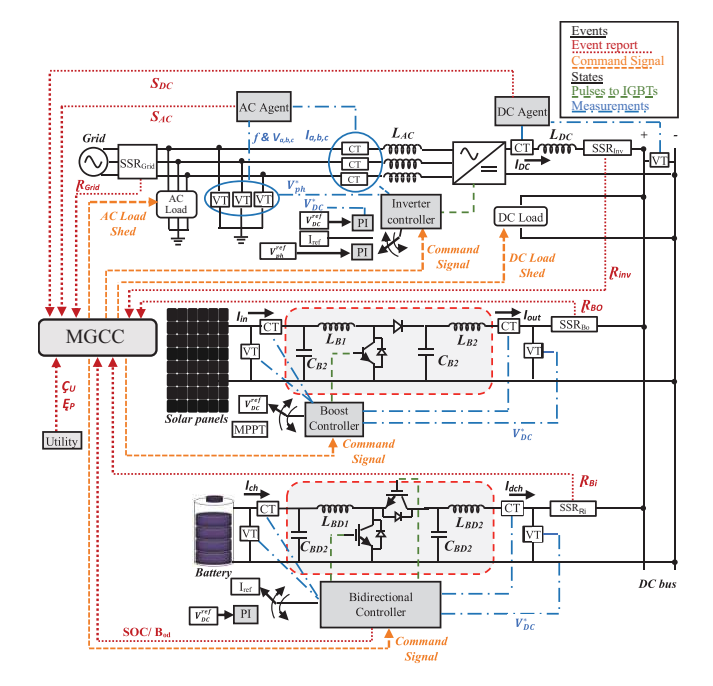


Fig. 1. MG topology understudy.

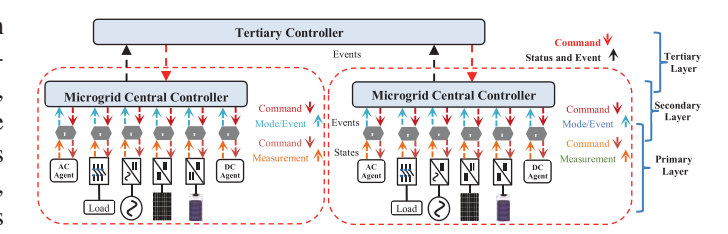


Fig. 2. Event and state driven Communication based control hierarchy.

occurs. This reduces the overall communication bandwidth requirement. According to [36] if the high bandwidth communication (HBC) sampling frequency is f_s , then the low bandwidth communication (LBC) sampling frequency is f_s/N (i.e., the amount of data on the communication network is reduced to 1 / N in LBC), where N is the number of control periods. Based on this, in this paper, the communication bandwidth has been further reduced between the MGCC and the LCs. During operation, no communication happens unless an event occurs (i.e., an LC signal is sent to the MGCC only if a new event occurs). In other words, according to [27] if the total sampling time during the control process $T_s = \sum_{0}^{N_s-1} T_{N_s}$, where N_s is the number of samples sent through the communication network during the control process and T_{N_s} is the sample time of one sample of N_s . Therefore, assuming all samples have the same duration then in HBC T_s is higher than that in LBC. However, in event driven control $T_s|_e = \sum_{0}^{m-1} T_{N_s}$, where m is the number of events triggered during the control process. Since events do not occur constantly then $T_s|_{e}$ is considerably low compared to T_s in HBC and LBC, as will be shown in Section III, which reduces the communication bus load and the computational cycle. This paper introduces a framework for communication-based microgrid control using finite state machine. Even though we chose to deploy a heuristic technique, mathematical based techniques can be also used.

The tertiary control layer may share some functions with the secondary one. It typically refers to the control layer coordinating multiple microgrids. It is often considered a part of the utility control center, or a third party, beyond an individual microgrid. This control layer is outside the scope of this paper. In the rest of the paper, "state driven control" will refer to the time driven control and each "mode" will describe the operational conditions of the microgrid.

III. OPERATIONAL MODES AND TRANSITIONS

The control scheme of the MGCC for the D1 configuration consists of a core layer, which encompasses five modes: (1) grid-tied (energy saving) mode (M₀₀) that is assumed to be the initial mode; (2) islanding mode (M_{01}) ; (3) emergency mode (M_{02}) ; (4) utility mode (M_{03}) ; and (5) shutdown mode (M_{04}) , as shown in Fig. 3. The MGCC has been designed to trigger only one transition at a time. The MGCC stores the last signaled event from the agents, relays, and LCs. The MGCC triggers a new transition based on the most recent event and the stored events. All triggering signals (C_{U} , S_{AC} , S_{DC} , \mathcal{R}_{inv} , \mathcal{R}_{Grid} , \mathcal{R}_{Bi} , \mathcal{R}_{Bo} , SOC, P, and B_{od}) are either one or zero, where "0" indicates normal operation and "1" indicates the opposite. For example, when \mathcal{R}_{Grid} is "1," this means that the circuit breaker (CB) is open at the PCC and the MG is islanded. When it is "0," it indicates normal operation.

A. Core Mode

Within this layer, transitions between the main modes take place. For instance, the initial mode is M_{00} , if a grid outage happens and SSR_{Grid} reports it ($\mathcal{R}_{Grid}=1$), or the AC agent signals AC voltage/frequency violation ($S_{AC}=1$), a transition to M_{10} will happen. However, if the SSR_{Inv} reports a fault ($\mathcal{R}_{Inv}=1$), a transition to M_{20} will occur. In case the utility sends a signal to take over the control of the MG ($\mathcal{C}_{U}=1$), according to a predefined agreement, and all the MG resources are available, a transition to M_{30} will occur. If all the resources are not available at any given instant, a transition to M_{40} will happen. More transitions might happen among the other modes within this layer, subject to the triggering events, which can be observed in blue lines in Fig. 3. Each mode comprises some sub-modes that will be discussed herein.

B. Grid-Tied/Energy Saving Mode

 M_{00} is the initial mode of the entire FSM. The objective of heuristic logic implemented in this mode is to maintain economic operation, by managing energy exchange with the main grid. Transitions within M_{00} are triggered by \mathcal{E}_P , \mathcal{R}_{Bi} and SOC of the battery. Starting from m_{00} , the MGCC commands the LC_{Inv} to regulate the DC bus voltage, LC_{Bo} to perform maximum power point tracking (MPPT) and LC_{Bi} to be neutral, i.e., current control with $I_{ref} = 0$. If the energy price signal becomes low ($\mathcal{E}_P = 1$), the MGCC checks the last status of LC_{Bi} to confirm that the battery is not full (SOC = 1), and the

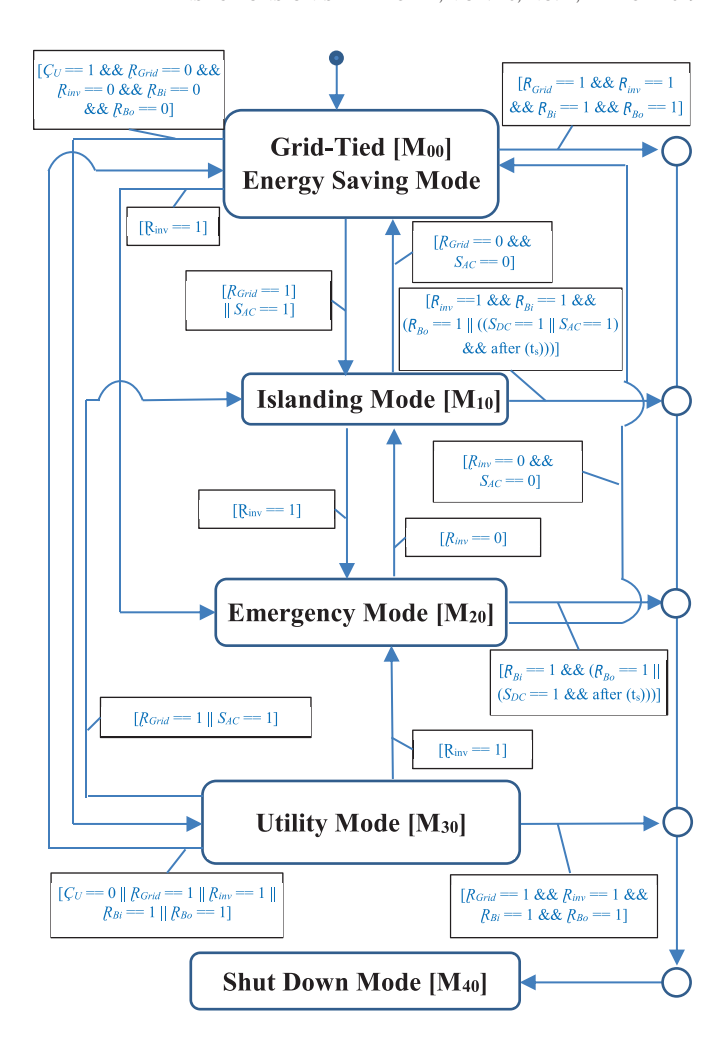


Fig. 3. Control logic/state flow chart of FSM of the core mode.

SSR_{Bi} to assure no fault operation ($\mathcal{R}_{Bi} = 0$), then a transition to m_{01} takes place. Within m_{01} , the LC_{Bi} starts charging the battery system with I_{1c} , to exploit the advantage of low energy price, while the LC_{Inv} and LC_{Bo} are still maintaining the same operation from m_{00} . However, if the energy price signal is high ($\mathcal{E}_P = 0$), the SSR_{Bi} last report states that there is no fault operation ($\mathcal{R}_{Bi} = 0$), and the LC_{Bi} last signal reports that the battery has the capability to discharge (SOC = 0), a transition to m_{02} happens. In order to increase the economic savings during m_{02} , LC_{Bi} starts discharging with I_{1c} . The rest of transitions can be observed from Fig. 4.

C. Islanding Mode

 M_{01} is either triggered when SSR_{Grid} signals power outage ($\mathcal{R}_{Grid}=1$), or when the AC agent reports voltage/frequency deviations beyond the permissible limits ($S_{AC}=1$). M_{01} contains four sub-modes: (1) islanding (m_{10}); (2) contingency (m_{11}); (3) critical (m_{12}); and (4) extreme (m_{13}). Starting from the initial sub-mode m_{10} , shown in Fig. 5, the MGCC triggers the first level of AC and DC load shedding, commands LC_{Inv} to maintain the AC bus voltage and frequency, LC_{Bo} to operate as MPPT, and LC_{Bi} to fix the DC bus voltage. If the SSR_{Bi} detects a fault where it is located, e.g., due to abnormal operation of the bidirectional converter or a fault, and

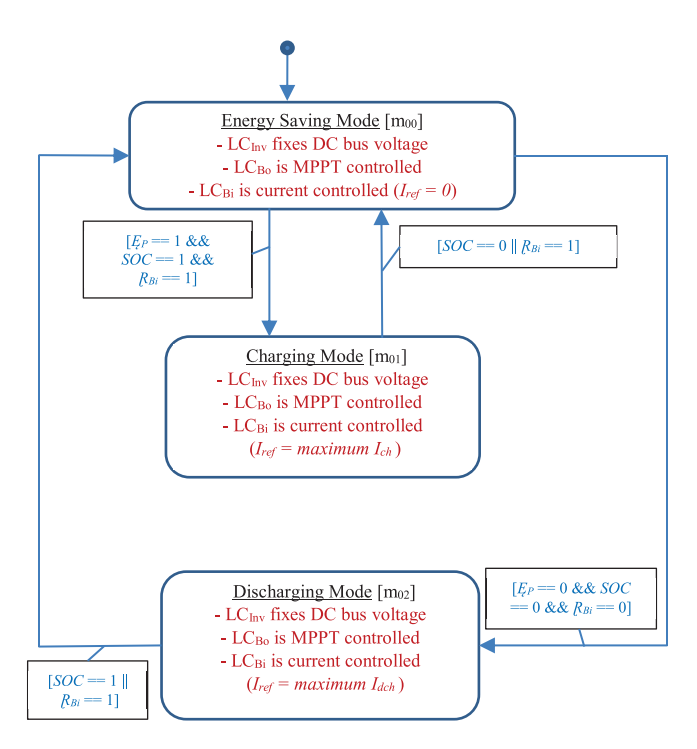


Fig. 4. Control logic/state flow chart of FSM of the grid-tied/energy saving mode.

reports it ($\mathcal{R}_{Bi} = 1$), a transition to m_{13} will happen. Within m₁₃, LC_{Bo} maintains the DC bus voltage, and a maximum level of load shedding will be triggered, which means almost \sim 5-10% of the total load will be supplied. The type of load connected at this level of load shedding should be tolerable to some voltage variations, due to photovoltaic generation intermittency. If the DC or AC agents signal significant deviation during m_{13} ($S_{DC} = 1$ or $S_{AC} = 1$), a transition to M_{04} will take a place to protect the loads as shown in Fig. 3. Another example, starting from m_{10} , if the LC_{Bi} signals battery depletion (SOC = 1), and LC_{Bo} was still available, according to the last report received from the SSR_{Bo} ($\mathcal{R}_{Bo} = 0$), a transition to m₁₁ will occur. During this mode, a different level of load shedding will take place, such that a portion of the solar energy available is used to charge the batteries with a maximum of half I_{1c} . The reason for charging the batteries is to maintain continuous operation of loads for as long as possible. The rest of the energy is utilized to supply the remaining loads. The amount of charging current, 0.5 I_{1c} , was selected based on the amount of critical loads that needs to be supplied in this mode. This happens while LC_{Bo} is MPPT controlled, and LC_{Bi} still maintains the DC bus voltage. On the other hand, also starting from m₁₀, if solar fluctuations occur while LC_{Bi} is maintaining the DC bus voltage, the battery system might exceed I_{1c} to keep supplying the loads. If over discharging lasts for a time interval that is greater than the settling time of the nested PI of the LC_{Bi} ($B_{od} = 1$), or the SSR_{Bo} signals the tripping of the boost convert ($\mathcal{R}_{BO} = 1$), then a transition to m_{12} will take place. The reason behind considering the settling time within the transition condition is to guarantee that the voltage oscillations resulting from the LCBi do not falsely trigger a new sub-mode. Nevertheless, more time could be added to

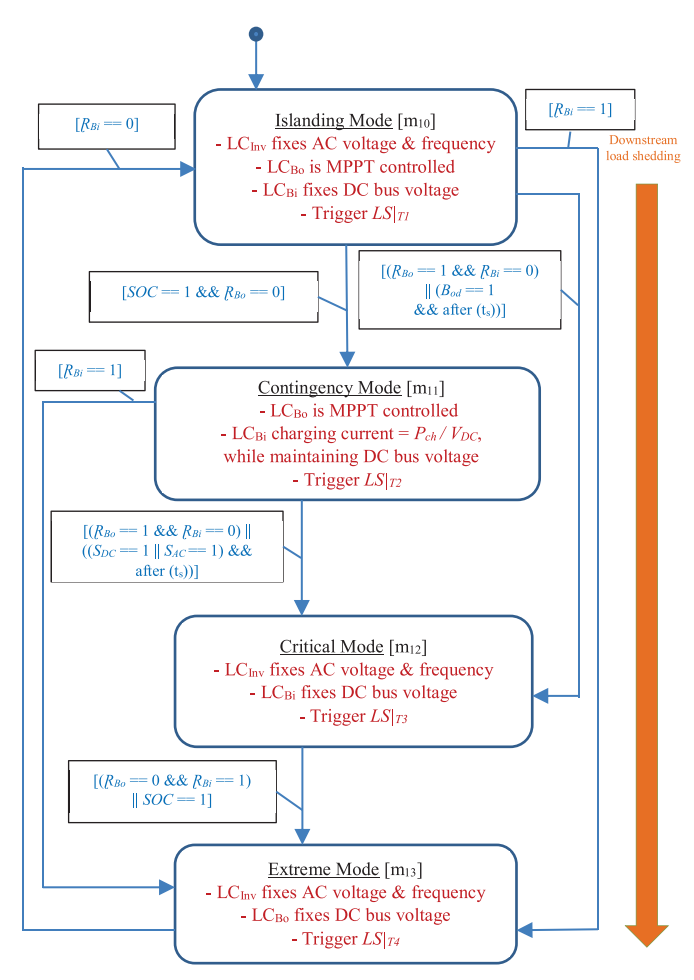


Fig. 5. Control logic/state flow chart of FSM of the islanding mode.

this condition as a safety margin, to further assure that the transition is not due to temporary solar fluctuations. The rest of the transitions could be observed in Fig. 5.

There are four levels of load shedding within M_{01} and M_{02} modes. They are selected based on the emergency loads, the available resources at the instant of load shedding, and a margin of safety to account for solar intermittency. For instant, the first level:

$$LS_T|_1 = P_D - (P_{Res}|_{Lst1} - P_m)$$
 (1)

$$LS_T|_1 = P_{DC1}^{LS}(m) * LS_{DC}|_1 + m_{10} * LS_{AC}|_1$$
 (2)

$$P_{DC1}^{LS}(m) = \sum_{i=1}^{2} m_{i,0} = \begin{cases} 1 & (\exists m_{i,j} \in M) P_{DC1}^{LS}(m) = 1 \\ 0 & (\forall m_{i,j} \in M) P_{DC1}^{LS}(m) = 0 \end{cases}$$
(3)

$$P_{Res}|_{Lst1} = P_b + P_{PV}|_{Lst1} \tag{4}$$

where $LS_{DC}|_1$, $LS_{AC}|_1$ are based on predefined load priority. P_m is a factor that accounts for the uncertainty of solar power during islanding. A good estimation for P_m can be achieved if photovoltaic power production history at the MG location is available. The second level of load shedding takes place when the batteries are depleted. A portion of the PV power is utilized to charge the battery system. The second level of load shedding could be represented as follows:

$$LS_T|_2 \le P_D - \left(P_{pv}\big|_{Lst2} - P_{ch}\right) \tag{5}$$

$$LS_T|_2 = P_{DC2}^{LS}(m) * LS_{DC}|_2 + m_{11} * LS_{AC}|_2$$
 (6)

$$P_{DC2}^{LS}(m) = \sum_{i=1}^{2} m_{i,1} = \begin{cases} 1 & (\exists m_{i,j} \in M) P_{DC2}^{LS}(m) = 1\\ 0 & (\forall m_{i,j} \in M) P_{DC2}^{LS}(m) = 0 \end{cases}$$
(7)

where P_{ch} equals the remaining power available after supplying the important loads. $LS_{T|2}$ depends on the priority of the remaining loads, and the time of the day, i.e., if it is close to sunset, P_{ch} will be high, so that the batteries can maintain supporting some of the loads after sunset. The third level of load shedding occurs when the boost converter is tripped or it is sunset. Load shed is executed such that the connected loads power is equal to the power that the battery system can supply, therefore:

$$LS_T|_3 \le P_D - P_b \tag{8}$$

$$LS_T|_3 = P_{DC3}^{LS}(m) * LS_{DC}|_3 + m_{12} * LS_{AC}|_3$$
 (9)

$$P_{DC3}^{LS}(m) = \sum_{i=1}^{2} m_{i,2} = \begin{cases} 1 & (\exists m_{i,j} \in M) P_{DC2}^{LS}(m) = 1 \\ 0 & (\forall m_{i,j} \in M) P_{DC2}^{LS}(m) = 0 \end{cases}$$
(10)

The last level of load shedding happens when the bidirectional converter is tripped and the boost converter is still available. At this level of load shedding, it is preferable to keep only a minimal portion of the load, which has the capability to handle a wide range of voltage variations to mitigate power fluctuations due to solar intermittency.

$$LS_T|_4 \le \sim 10 - 20\% \text{ of } P_{pv}|_{Lst4}$$
 (11)

$$LS_T|_4 = P_{DC4}^{LS}(m) * LS_{DC}|_4 + m_{13} * LS_{AC}|_4$$
 (12)

$$P_{DC4}^{LS}(m) = \sum_{i=1}^{2} m_{i,2} = \begin{cases} 1 & (\exists m_{i,j} \in M) P_{DC4}^{LS}(m) = 1 \\ 0 & (\forall m_{i,j} \in M) P_{DC4}^{LS}(m) = 0 \end{cases}$$
(13)

This logic has been prepared to have unidirectional downstream load shedding during M_{01} and M_{02} modes, i.e., no reconnection of loads happens unless normal operation is restored, to preserve the safety of the loads.

D. Emergency Mode

 M_{20} represents complete isolation between the AC and DC buses. The objective of this mode is to maintain a reliable supply of energy to the emergency loads connected to the DC bus for as long as possible. M_{20} contains the following submodes: emergency (m_{20}) , contingency (m_{21}) , critical (m_{22}) , and extreme (m_{23}) . M_{20} is similar to the islanding mode M_{10} , except for, it has only DC load shedding and a DC agent monitoring the DC bus, to report any violations of the DC bus voltage beyond the acceptable limits to the MGCC. The transition conditions can be observed from Fig. 6. Moreover, detailed Tables A.II, A.III, A.IV and A.V in the Appendix, list all possible transitions in all modes.

Observing Figs. 1, 5 and 6, Tables A.IV and A.V in the Appendix, and the above discussion, it can be concluded that within D2, the islanding mode will be canceled out and replaced by the emergency mode to island the MG. Since in

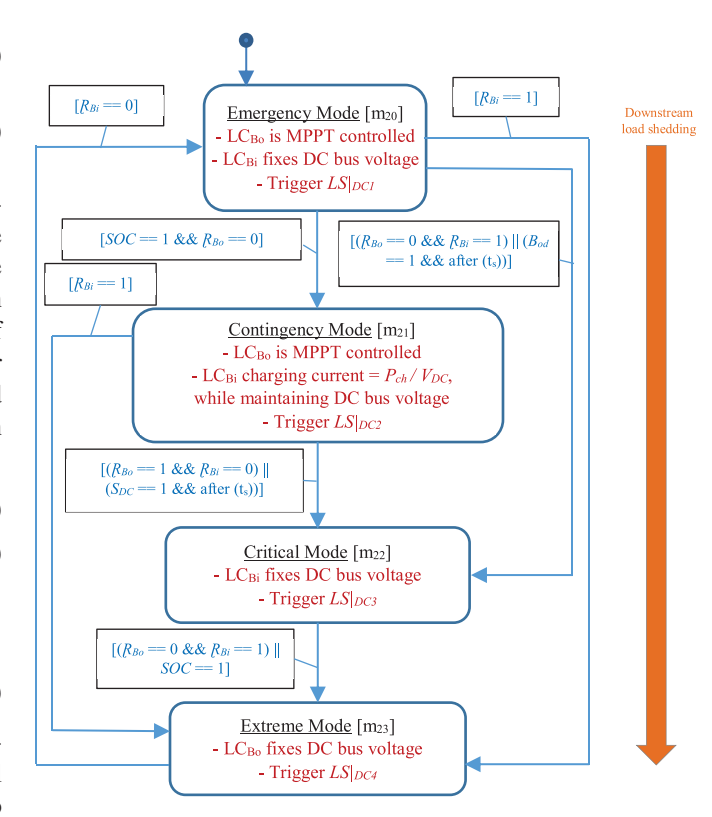


Fig. 6. Control logic/state flow chart of FSM of the emergency Mode.

D2, all the MG loads are located within the DC MG and connected to the DC bus, then the AC and DC sides will be completely isolated, in case SSR_{Inv} signals its circuit breaker to open due to a fault. Therefore, the islanding mode will not be required.

E. Utility and Shutdown Modes

The goal of the utility mode M_{03} , is for the utility to take control over the MG, e.g., to virtually aggregate multiple MGs on a feeder, or enhance the voltage level (of the distribution feeder) by asking microgrids to inject reactive power. As for the shutdown mode M_{04} , its objective is to guarantee a shutdown in case all resources were disconnected or became unavailable at any given moment. Moreover, if the permissible limits of AC or DC voltage and/or frequency are violated during m_{13} or m_{23} , a transition to M_{04} happens, in order not to jeopardize the safety of the loads.

IV. FINITE STATE MACHINE ANALYSIS

The design of the control scheme for the microgrid can be conceptualized in terms of a finite state machine (FSM). FSM is a mathematical model used to develop a logical process. It can be thought of as a machine with a finite number of operational conditions called states. The machine can only be in one state at a time and can transition to another state based on single or multiple events. Therefore, designing the control logic is a matter of defining the states and deciding on the events which cause the states to transition from the current state to the next. In our case, the machine and states are the MG and modes, respectively.

Local controller	Mode	State variables
DC/DC boost	MPPT	$V_{pv} \ I_{pv}$
converter	Voltage control	V_{out}^{bo}
DC/DC bidirectional	Current control	$I_{in}^{bi} \ I_{out}^{bi}$
converter	Voltage control	V_{out}^{bi}
AC/DC inverter	Current/Voltage control	v_a, v_b, v_c i_a, i_b, i_c

TABLE II EVENTS AND COMMANDS COMMUNICATED WITH THE MGCC

Agent/LC/ SSR	Event	Triggering variable
Bidirectional	Battery depleted	SOC
converter	Over discharge	B_{od}
AC Agent	AC voltage/Frequency deviations	v_a, v_b, v_c, f
DC Agent	DC voltage deviations	V_{DC}
Inverter SSR	Inverter is tripped	R_{inv}
Boost SSR	Boost converter is tripped	R_{Bo}
Bidirectional SSR	Bidirectional converter is tripped	R_{Bi}
Grid SSR	Blackout	R_{Grid}
Utility	High/Low energy price	E_{P}
MGCC	DC load shedding command	Dependent on the
MOCC	AC load shedding command	present mode

In this section, correlations between the event-driven modes in the secondary layer and the conventional LCs PI time-driven control in the primary control layer will be developed using FSM. The FSM mathematical models for the DC MG primary and secondary control layers, including the state variables and events will be derived. For the DC MG shown in Fig. 1, each LC is maintaining its local mode, i.e., neutral, voltage or current control mode, by monitoring and controlling the state variables of its converter, e.g., the input and output currents. The local mode of each LC is being triggered by a command signal from the MGCC, based on triggering event/s, and the predefined logic (i.e., control scheme) implemented in the MGCC. Tables I and II show the state variables and events for the DC MG.

The FSM for the DC MG control could be represented by the following variables (\sum , M, m₀₀, δ), where:

- ∑: is a finite set of inputs to the MGCC, which are the events in Table II.
- M: is a finite, non-empty set of modes, M comprises all mode sets:
 - M_{00} (Grid-tied/Energy saving 1 mode)= $\{m_{00}, m_{01}, m_{02}\}$, such that $\forall m_{0j} \ (m_{0j} \in M_{00} \rightarrow m_{0j} \in M)$ where j = 0, 1, 2.
 - M_{10} (Islanding mode)= $\{m_{10}, m_{11}, m_{12}, m_{13}\}$, such that $\forall m_{1j} (m_{1j} \in M_{10} \rightarrow m_{1j} \in M)$ where j = 0, 1, 2, 3.
 - M_{20} (Emergency mode)= $\{m_{20}, m_{21}, m_{22}, m_{23}\}$, such that $\forall m_{2j} (m_{2j} \in M_{20} \rightarrow m_{2j} \in M)$ where j = 0, 1, 2, 3.

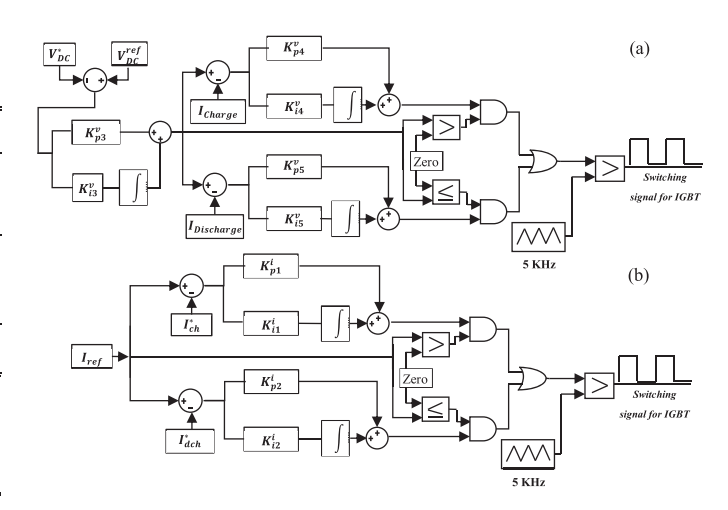


Fig. 7. Bidirectional converter local controller: a) voltage control mode, b) current control mode.

- M_{30} (Utility mode)= $\{m_{30}\}$, such that $m_{30} \in M$.
- M_{40} (Shutdown mode) = $\{m_{40}\}$, such that $m_{40} \in M$.

Therefore $M = \{M_{00}, M_{01}, M_{02}, M_{03}, M_{04}\}$, which was explained in Section III.

- m_{00} : is the initial mode of the state machine, $m_{00} \in M$.
- δ: is the mode transition function, δ: M × ∑ → M, it is described in details in the Appendix.

The FSM implementation between the LCs and the MGCC, will be described for each LC as follows.

A. DC/DC Bidirectional Converter Local Controller

The bidirectional converter local controller (LC_{Bi}) can operate in a neutral, voltage, or current control mode. For current control mode, two PI controllers were implemented to achieve a desired current reference, for the charging and discharging modes as shown in Fig. 7(b). As for the voltage control, a nested PI was implemented as shown in Fig. 7(a). The values of K_p and K_i for both controllers are shown in the Appendix, Table A.VI. The transfer function for the LC_{Bi} , using the FSM could be derived as follows:

The transfer function for the charging current control is:

$$G_{ch}(S) = K_{p1}^{i} \left(I_{ch}^{ref} - I_{ch}^{*} \right) + \frac{K_{i1}^{i}}{s} \left(I_{ch}^{ref} - I_{ch}^{*} \right)$$
(14)

The transfer function for the discharging current control is:

$$G_{dch}(S) = K_{p2}^{i} \left(I_{dch}^{ref} - I_{dch}^{*} \right) + \frac{K_{i2}^{i}}{s} \left(I_{dch}^{ref} - I_{dch}^{*} \right)$$
 (15)

The transfer function of the outer loop for voltage control is:

$$G_{\nu}^{bi}(S)\Big|_{ol} = K_{p3}^{\nu} \Big(V_{DC}^{ref} - V_{DC}^* \Big) + \frac{K_{i3}^{\nu}}{s} \Big(V_{DC}^{ref} - V_{DC}^* \Big) \quad (16)$$

In the nested PI controller, the outer loop yields the reference for the inner loop. Therefore, by substituting (16) in (14) and (15), the nested PI controller transfer function,

for maintaining the DC bus voltage will be:

$$G_{\nu}^{bi}(S) = \begin{cases} P_{\nu}^{bi}(m) * \begin{pmatrix} K_{p4}^{\nu} (G_{\nu}(S) - I_{ch}^{*}) + \\ \frac{K_{p4}^{\nu}}{s} (G_{\nu}(S) - I_{ch}^{*}) \end{pmatrix} V_{DC} > V_{ref} \\ P_{\nu}^{bi}(m) * \begin{pmatrix} K_{p5}^{\nu} (G_{\nu}(S) - I_{dch}^{*}) + \\ \frac{K_{i5}^{\nu}}{s} (G_{\nu}(S) - I_{dch}^{*}) \end{pmatrix} V_{DC} < V_{ref} \end{cases}$$
(17)

From Figs. 5 and 6:

$$P_{\nu}^{bi}(m) = \sum_{j=0}^{2} \sum_{i=1}^{2} m_{i,j} = \begin{cases} 1 & (\exists m_{i,j} \in M) P_{\nu}^{bi}(m) = 1 \\ 0 & (\forall m_{i,j} \in M) P_{\nu}^{bi}(m) = 0 \end{cases}$$
(18)

And from (14) and (15), the PI transfer function for charging/discharging the batteries through the bidirectional converter is:

$$G_{i1}^{bi}(S) = \begin{cases} P_{i1}^{bi}(m) * \left(K_{p1}^{i} \left(I_{ref} - I_{ch}^{*} \right) + \frac{K_{i1}^{i}}{s} \left(I_{ref} - I_{ch}^{*} \right) \right) I_{ref} > 0 \\ P_{i2}^{bi}(m) * \left(K_{p2}^{i} \left(I_{ref} - I_{dch}^{*} \right) + \frac{K_{i2}^{i}}{s} \left(I_{ref} - I_{dch}^{*} \right) \right) I_{ref} \le 0 \end{cases}$$

$$(19)$$

where a single current reference is used. Depending on the sign of the reference current, the LC_{Bi} switches between charging and discharging modes.

From Fig. 4:

$$P_{i1}^{bi}(m) = m_{01} = \begin{cases} 1 & (\exists m_{i,j} \in M) P_{i1}^{bi}(m) = 1\\ 0 & (\forall m_{i,j} \in M) P_{i1}^{bi}(m) = 0 \end{cases}$$
(20)
$$P_{i2}^{bi}(m) = \sum_{i=0}^{1} m_{0,2i} = \begin{cases} 1 & (\exists m_{i,j} \in M) P_{i2}^{bi}(m) = 1\\ 0 & (\forall m_{i,j} \in M) P_{i2}^{bi}(m) = 0 \end{cases}$$

 $i2^{(m)} = \sum_{i=0}^{m_{0,2i}} m_{0,2i} = \begin{cases} 0 & (\forall m_{i,j} \in M) P_{i2}^{bi}(m) = 0 \end{cases}$ (21)

Therefore, from (17) and (19), the complete transfer function with FSM of the bidirectional local control is:

$$G_T^{bi}(s) = G_V^{bi}(s) + G_i^{bi}(s)$$
 (22)

It can be noticed from (14) through (22), that the state variables of the LC_{Bi} to maintain its various modes are the input/output currents and the output voltage of the bidirectional converter. Moreover, it can be seen that the set of event-driven modes, $\{m_{20}, m_{22}, m_{10}, m_{12}, m_{21}, m_{11}, m_{01}, m_{02}\} \subseteq M$, commanded by the MGCC will have a direct impact on the operation of the LC_{Bi} .

B. Boost Converter Local Controller

The boost converter local controller (LC_{Bo}) could function either as MPPT or voltage regulator, as shown in Fig. 8. The values for K_p and K_i are shown in the Appendix, Table A.VI. The transfer function for the LC_{Bo} can be derived similarly as was shown above:

$$G_{\nu}^{bo}(S) = K_{p6}^{\nu} \left(V_{DC}^{ref} - V_{DC}^{*} \right) + \frac{K_{i6}^{\nu}}{s} \left(V_{DC}^{ref} - V_{DC}^{*} \right)$$
 (23)

$$G_T^{bo}(S) = P_i^{bo}(m) * MPPT(S) + P_v^{bo}(m) * G_v^{bo}(S)$$
 (24)

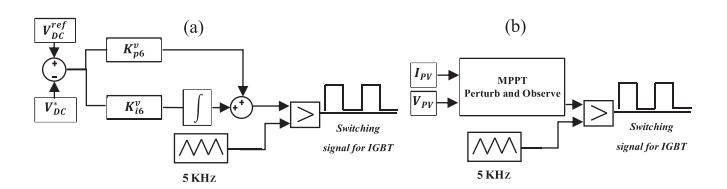


Fig. 8. Boost converter local controller: a) voltage control mode, b) MPPT control mode

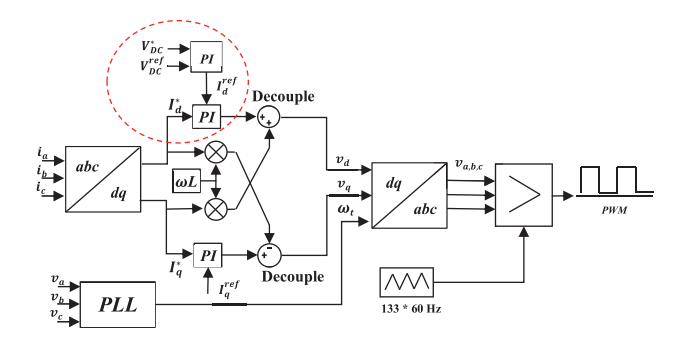


Fig. 9. Inverter local controller to maintain the DC bus voltage.

From Figs. 4, 5 and 6:

$$P_{i}^{bo}(m) = \sum_{j=0}^{2} \sum_{i=0}^{2} m_{i,j} = \begin{cases} 1 & (\exists m_{i,j} \in M) P_{i}^{bo}(m) = 1 \\ 0 & (\forall m_{i,j} \in M) P_{i}^{bo}(m) = 0 \end{cases}$$
(25)

$$P_{\nu}^{bo}(m) = \sum_{i=1}^{2} m_{i,3} = \begin{cases} 1 & (\exists m_{i,j} \in M) P_{\nu}^{bo}(m) = 1 \\ 0 & (\forall m_{i,j} \in M) P_{\nu}^{bo}(m) = 0 \end{cases}$$
(26)

For the LC_{Bo} , the state variables are the voltage and current of the solar panel, and the output voltage of the boost converter as shown in Table I. The modes that trigger the MPPT are $\{m_{00}, m_{01}, m_{02}, m_{10}, m_{11}, m_{12}, m_{20}, m_{21}, m_{22}\} \subseteq M$, and those that trigger voltage control are $\{m_{13}, m_{23}\} \subseteq M$.

C. Inverter Local Controller

The inverter local controller (LC_{Inv}) is considered the primary responsible when it comes to maintaining the DC bus voltage, as shown in Fig. 9. v_{abc} is measured from the utility grid side to acquire the voltage, phase and frequency using a phase locked loop (PLL) to enable synchronization with the main grid. The inverter output currents in the abc frame of references are converted to dq0 frame of references, and regulated through PI controllers. Then, the reference dq voltages, after decoupling, are used to generate the modulation signals. I_d is regulated through another PI, which has an input of $(V_{DC}^{ref} - V_{DC}^*)$, to maintain DC bus voltage. If a grid outage occurs, the microgrid islands itself, and the LC_{Inv} receives a signal from the MGCC to maintain the AC bus voltage and frequency, as long as the inverter is still connected to the DC bus (i.e., not tripped). In this mode, the LC_{Inv} compares the RMS value of the phase voltage of the AC load with an arbitrary 120 V, 60 Hz sine wave reference signal through a PI controller to create the modulation signal. This modulation signal is then compared with a saw-tooth signal, to generate the pulses for the IGBTs of the inverter. Moreover, The LC_{Inv}

could operate in a current control mode, if an I_D^{ref} replaces the outer voltage PI loop, as shown in Fig. 9. LC_{Inv} may operate with current control in case the utility takes control over the MG. The values of K_p and K_i for the LC_{Inv} various modes, are shown in the Appendix, Table A.VI.

The transfer function for the inverter AC voltage controller with FSM will be as follows:

$$G_{ac}^{inv}(S) = P_{ac}^{inv}(m) * \begin{pmatrix} K_{p7}^{ac} (V_{ref}^{ph} - V_{ph}^*) \\ + \frac{K_{ref}^{iac}}{s} (V_{ref}^{ph} - V_{ph}^*) \end{pmatrix}$$
(27)

From Fig. 5:

$$P_{ac}^{inv}(m) = \sum_{j=0}^{3} m_{1,j} = \begin{cases} 1 & (\exists m_{i,j} \in M) P_{ac}^{inv}(m) = 1 \\ 0 & (\forall m_{i,j} \in M) P_{ac}^{inv}(m) = 0 \end{cases}$$
(28)

The transfer function for the Inverter DC voltage controller, the outer loop, will be as follows:

$$G_{DC}^{inv}(S)\big|_{ol} = K_{p8}^{DC}(V_{DC}^{ref} - V_{DC}^*) + \frac{K_{i8}^{DC}}{s} \left(V_{DC}^{ref} - V_{DC}^*\right)$$
(29)

The nested PI controller transfer function, for maintaining the DC bus voltage with FSM will be:

$$G_{DC}^{inv}(S) = P_{DC}^{inv}(m) * \begin{pmatrix} K_{p9}^{DC}(G_{DC}^{inv}(S)|_{ol} - I_d^*) \\ + K_{i9}^{DC}(G_{DC}^{inv}(S)|_{ol} - I_d^*) \end{pmatrix}$$
(30)

From Fig. 4:

$$P_{DC}^{inv}(m) = \sum_{i=0}^{2} m_{0,j} = \begin{cases} 1 & (\exists m_{i,j} \in M) P_{DC}^{inv}(m) = 1 \\ 0 & (\forall m_{i,j} \in M) P_{DC}^{imv}(m) = 0 \end{cases}$$
(31)

Also, the transfer function for the inverter current controller, active and reactive current control, will be as follows:

$$G_{id}^{inv}(S) = P_i^{inv}(m) * \left(K_{p10}^{id} \left(I_d^{ref} - I_d^* \right) + \frac{K_{i10}^{id}}{s} \left(I_d^{ref} - I_d^* \right) \right)$$

$$G_{iq}^{inv}(S) = P_i^{inv}(m) * \left(K_{p11}^{iq} \left(I_q^{ref} - I_q^* \right) + \frac{K_{i11}^{iq}}{s} \left(I_q^{ref} - I_q^* \right) \right)$$
(32)

Since it takes place during utility mode M₀₃, then:

$$P_i^{inv}(\mathbf{m}) = \mathbf{m}_{30} = \begin{cases} 1 & (\exists \mathbf{m}_{i,j} \in \mathbf{M}) \mathbf{m}_{30} = 1\\ 0 & (\forall \mathbf{m}_{i,j} \in \mathbf{M}) \mathbf{m}_{30} = 0 \end{cases}$$
(34)

The complete transfer function with FSM for the inverter controller is:

$$G_T^{inv}(S) = G_{ac}^{inv}(S) + G_{DC}^{inv}(S) + G_{id}^{inv}(S) + G_{ia}^{inv}(S)$$
 (35)

The inverter state variables are the three-phase voltages of the grid, the three-phase output currents of the inverter, the phase and the frequency of the grid and the DC bus voltage. DC or AC voltage control for the LC_{Inv} will be activated in modes: $\{m_{00}, m_{01}, m_{02}, m_{10}, m_{11}, m_{12}, m_{13}\} \subseteq M$, while current control may only be activated in the utility mode, $m_{30} \in M$.

If the microgrid configuration is D2, all P(m) functions will be altered, such that, the islanding layer M_{10} and its modes would be removed $\{m_{10}, m_{11}, m_{12}, m_{13}\}$. The reason is that the emergency and islanding modes will be the same in D1, as explained in Section III.

V. RESULTS AND DISCUSSION

The proposed communication-based controller has been verified through various case studies. Selected cases, involving a series of transitions between modes/sub-modes, will be presented and discussed. Each case is presented by a set of four subplots. Each subplot has five segments, each segment reflects a new event or a set of events taking place. Subplot (a) of each figure presents DC currents for the inverter, boost converter, bidirectional converter, and DC load. Subplots (b), (c) and (d), depict the DC bus voltage, three phase AC currents from the inverter to the grid, and three phase AC voltages, respectively. All cases start with the assumed initial mode M₀₀, where LC_{Inv} is maintaining the DC bus voltage, LC_{Bo} operates as MPPT and LCBi is in a neutral state. A sampling frequency of 60 kHz was used (i.e., $T_{N_s} = \frac{1}{60.000} sec$). It will be noticed that a maximum of six events occurred in one of the following cases during 3.5 seconds time interval. During each event, only one to three LCs are communicating with the MGCC, depending on the type of event. Therefore, during operation: $T_s|_e = \frac{6}{60.000}$ * No. of the LCs communicating with the MGGC, which is considerably low compared to T_s in HBC and LBC that require constant communication signaling (i.e., constant back and forth communication) between all the LCs and the MGCC. This reduces the communication load and computational cycles significantly and consequently save energy.

A. Case I

This case demonstrates the control of the MGCC for D1 configuration of the DC MG in case of islanding. It shows the impact of solar intermittency on the transition between modes of operations, among other events. Segment (1) displays the transition from m₀₀ to m₁₀, due to a blackout being signaled by SSR_{Grid} ($\mathcal{R}_{Grid} = 1$). The first level of load shedding is triggered by the MGCC, reducing the AC and DC load currents as shown in Figs. 10(a) and 10(c), governed by (1). In addition, it can be observed that the inverter DC and AC currents changed their direction, (i.e., the grid was supplying the loads before the blackout). The inverter DC current becomes negative, also, the AC current magnitude decreases (i.e., load shedding was executed) as shown in Figs. 10(a) and 10(c), i.e., sending current/power to the AC loads instead of the grid. During m₁₀, the MGCC commands the inverter LC to maintain 120 V RMS AC bus voltage at 60 Hz, LCBi to maintain the DC bus voltage to 300 V, and LC_{Bo} to maintain operation with MPPT control, as derived in (22), (24) and (35). It can be noticed from Fig. 10(d) that the AC voltage started to be slightly distorted with ripples, due to the absence of the main grid. During segment (2), the solar intermittency caused the batteries to over discharge beyond 5 A (i.e., I_{1c}). The over

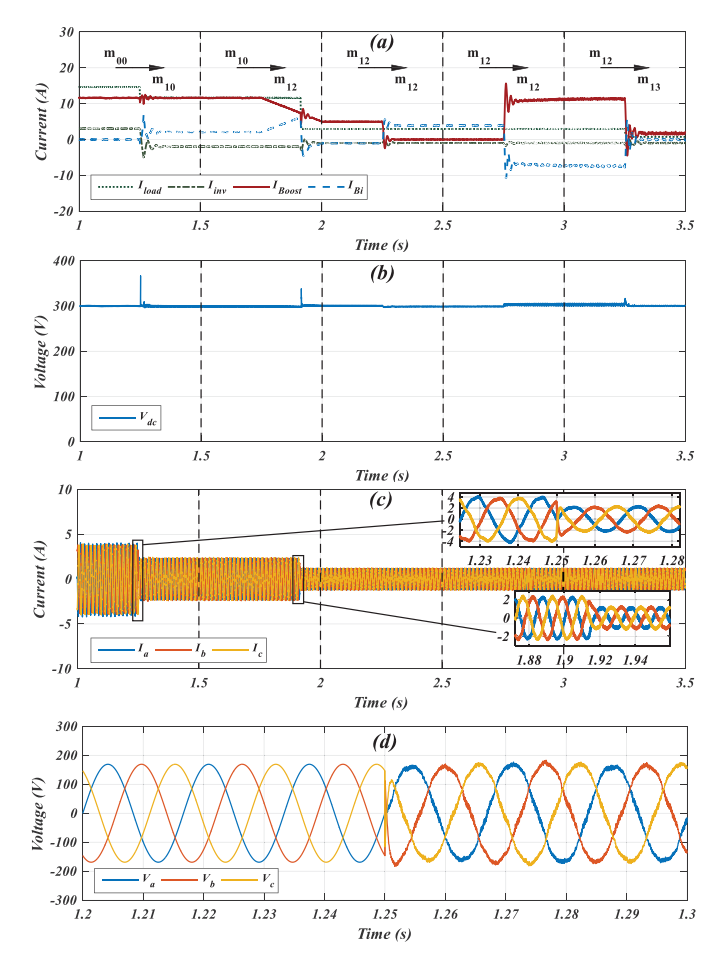


Fig. 10. Case I shows the operation of the MGCC for D1, during islanding mode.

discharging lasted for a time interval that is greater than the settling time of the nested PI of the LC_{Bi} (200 msec.). Consequently, B_{od} becomes one, signaled by LC_{Bi}, which triggers the transition to the critical sub-mode m₁₂. Within m₁₂, another level of AC and DC load shedding is introduced, which can be seen from the AC and DC load currents in Figs. 10(a) and 10(c), respectively, governed by (5). The LCs maintain the same duties in m_{12} as in m_{10} . During segments (3) and (4), the mode of operation is m_{12} . The boost converter is tripped in segment (3) and reconnected during segment (4). The LC_{Bi} reacted to maintain the DC bus voltage, i.e., discharged when the boost converter was tripped, and charged when it was reconnected. Throughout segments (3) and (4), the loads were not affected because during this mode, the load shedding is governed by (3), which is only a function of the battery power as discussed in Section IV. Segment (5) represents the tripping of the bidirectional converter, triggering the extreme mode m_{13} . This leads to the maximum load shedding, while the LCBo switches to voltage control, as derived in (24). It can be observed from Figs. 10(b) and 10(d) that the DC and AC bus voltages during all events were maintained within acceptable limits when using the proposed FSM logic to maneuver various critical scenarios.

B. Case II

Case II shows the operation of the MGCC for D2 during emergency mode M_{20} , showing the battery depletion impact on the performance of the MGCC, among other events. Segment (1) represents a transition from m_{00} to m_{20} due to a power outage from the grid side, signaled by SSR_{Inv} $(\mathcal{R}_{Inv} = 1)$. The AC currents and voltages dropped to zero as shown in Figs. 11(c) and 11(d) respectively. Since all loads are connected to the DC bus in this configuration, the MG will be islanded utilizing the emergency mode instead of the islanding mode as discussed earlier. During m₂₀, the MGCC triggers the first level of DC load shedding, which can be observed from the DC load current in Fig. 11(a) and governed by (1) and (2). LC_{Bi} is commanded to maintain the DC bus voltage to 300 V and LC_{Bo} to maintain MPPT, which can be expressed by (22) and (24). During segment (2), LC_{Bi} signals battery system depletion (SOC = 1); and since the SSR_{Bo} did not report any fault within the boost converter zone of protection ($\mathcal{R}_{Bo}=0$), a transition from m_{20} to m_{21} occurs. In m_{21} , the MGCC triggers $LS_{DC}|_2$ such that the battery system charges with 50% of I_{1c} (~2-3 A), while LC_{Bi} is still controlling the voltage, and LC_{Bo} operates with MPPT. At segment (3), the SSR_{Bo} signals the boost converter tripping $(\mathcal{R}_{Bo}=1)$. The MGCC confirms that the bidirectional converter is not tripped, since the SSR_{Bi} did not report any fault operation ($\mathcal{R}_{Bi} = 0$), leading to a transition from m_{21} to m_{22} . The MGCC trigger $LS_{DC}|_3$ in m_{22} , which can be seen in Fig. 11(a), where the load current reduces to be exactly equal to the bidirectional converter output current I_{1c} . The LC_{Bi} keeps carrying out the same task in m₂₂ as in m₁₂ maintaining the DC bus voltage. During segment (4), a reconnection for the boost converter was established. The battery receives the extra current/power as shown in Fig. 11(a). No load is allowed to reconnect during segment (4) to avoid excessive load shedding and reconnection to preserve load safety. Finally, segment (5) represents tripping of the bidirectional converter ($\mathcal{R}_{Bi} = 1$), leading to transition to m_{24} . The MGCC executes the maximum DC load shedding $LS_{DC}|_4$, while LC_{Bo} switches to voltage control, as derived in (24). Moreover, it can be noticed from Fig. 11(a) that the DC load current dropped to 20% of $P_{pv}|_{Lst4}$, and became exactly equal to the boost converter output current. Fig. 11(b) shows that the DC bus voltage was maintained to 300 V during all modes.

C. Case III

Case III illustrates the operation of the MGCC in D1, during the grid-tied/energy saving mode M_{00} . During segment (1), a signal is sent by the utility to the MGCC, informing it that the energy price is low ($\mathcal{E}_P = 1$). The MGCC checks the last SOC of the battery system through the latest signal received from the LC_{Bi} confirming it is not full (SOC = 1), and the last status of SSR_{Bi} assuring normal operation ($\mathcal{R}_{Bi} = 0$), which leads the MGCC to trigger the m_{01} sub-mode. Within m_{01} , each converter LC maintains the same task, except for LC_{Bi}, which initiates maximum charging ($I_{ref} = I_{1c}$), using current control as derived in (19). It can be noticed during

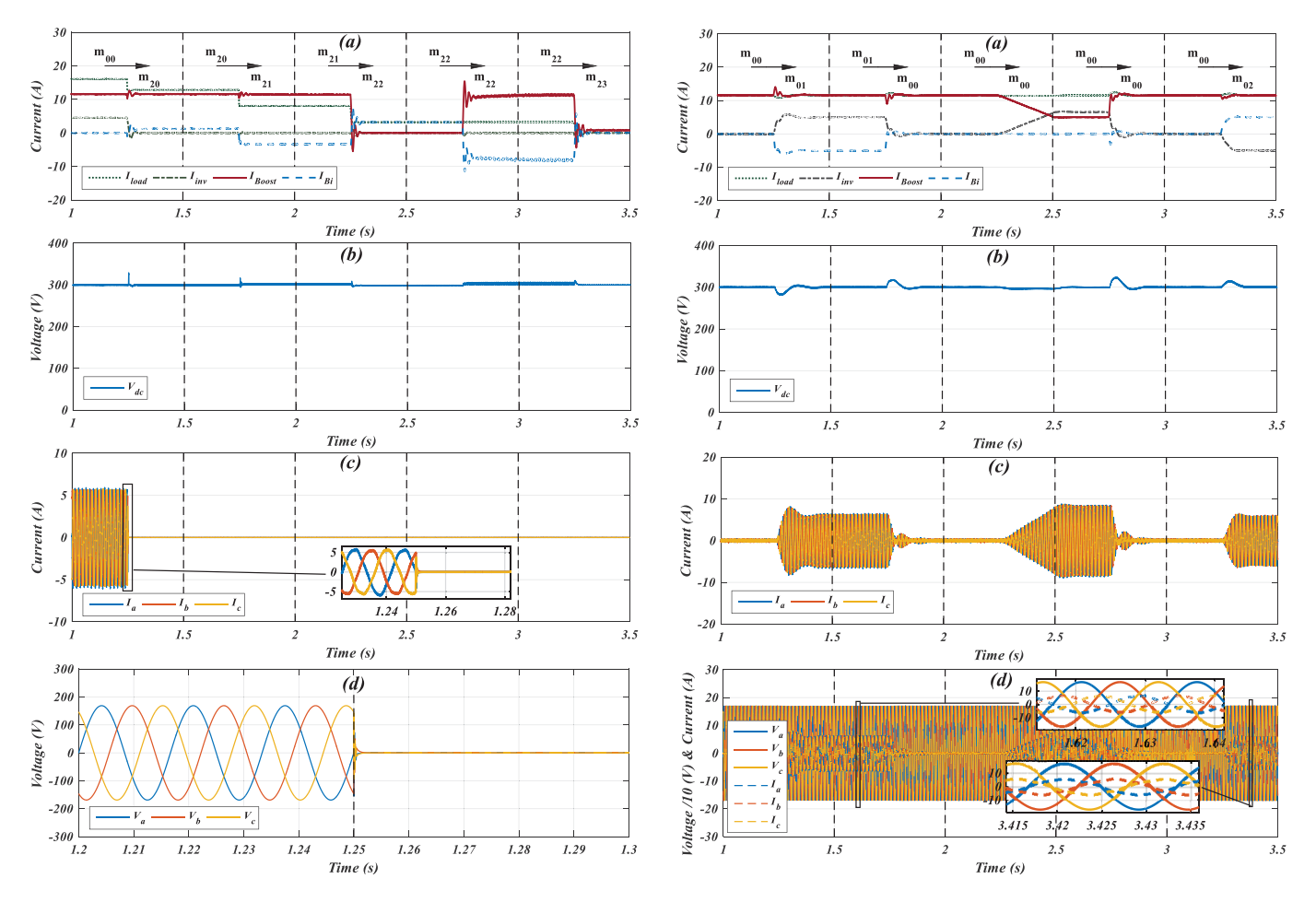


Fig. 11. Case II shows the operation of the MGCC for D2, during emergency mode.

Fig. 12. Case III shows the operation of the MGCC for D1, during grid-tied/energy saving mode.

segment (1) in Fig. 12(a) that the bidirectional converter current becomes -5 A, i.e., charging with $I_{ref} = 5$ A; therefore, the inverter DC current increases to 5 amps to maintain the DC bus voltage to 300 V as shown in Fig. 12(b). Moreover, the AC current increases as well from the grid to the DC MG through the inverter, and becomes 180° phase shifted from the voltage as shown in Fig. 12(d). For the period of segment (2), LC_{Bi} signals that the battery system is fully charged (SOC = 0), then m_{00} is retained by the MGCC. The bidirectional converter output current drops to zero and that of the inverter as well, maintaining the DC bus voltage as shown in Figs. 12(a) and 12(b), since the DC MG can self-sustain its DC loads at that instant. Throughout segment (3), the mode of operation is m_{00} , solar fluctuations (e.g., a passing cloud) caused the boost converter output current to decrease gradually. The inverter DC/AC currents increase in order to maintain the DC bus voltage, which can be noticed in Figs. 12(a), 12(b) and 12(c), respectively. During segment (4), the solar irradiance goes back to the same value as in segment (1) and the boost converter output current as well, which can be shown in Fig. 12(a). The inverter DC/AC current drops to almost zero, maintaining the DC bus voltage, as shown in Figs. 12(b) and 12(c), respectively. During the last segment, the utility signals high-energy price to the MGCC ($\mathcal{E}_P = 0$). The MGCC confirms the availability of the bidirectional converter ($\mathcal{R}_{Bi} = 0$),

a transition from m_{00} to m_{02} takes place. Through m_{02} , LC_{Bi} switches to discharge, governed by (19), and starts the rated discharging current ($I_d = I_{1c}$) with 5 A. The inverter DC current drops to -5 A to maintain the DC bus voltage to 300 V, i.e., sending 5 A to the grid, and the AC current/voltage become in phase, as shown in Figs. 12(a), 12(b) and 12(d), respectively.

D. Case IV

Case IV represents a transition between grid-tied and islanding modes, followed by a transition to the emergency mode and its sub-modes. In segment (1), a power outage happens ($\mathcal{R}_{Grid}=1$), triggering a transition from m_{00} to m_{10} , same as the earlier cases. During segment (2), the LC_{Bi} signals that the battery system is depleted (SOC=1), and since the last status of the SSR_{Bo} was no fault ($\mathcal{R}_{Bo}=0$), a transition from m_{10} to m_{11} takes place. Similar to segment (2) in case II, the second level of load shedding is triggered by the MGCC, except that $LS_{T|2}$ is executed instead of only $LS_{DC|2}$. The load shedding takes place such that the battery system charges with 50% of I_{1c} (\sim 2-3 A). In m_{11} , LC_{Bi} regulates the DC bus voltage, LC_{Inv} maintains the AC bus voltage and frequency, and LC_{Bo} operates with MPPT. The bidirectional current becomes negative, receiving the extra current to maintain the DC bus

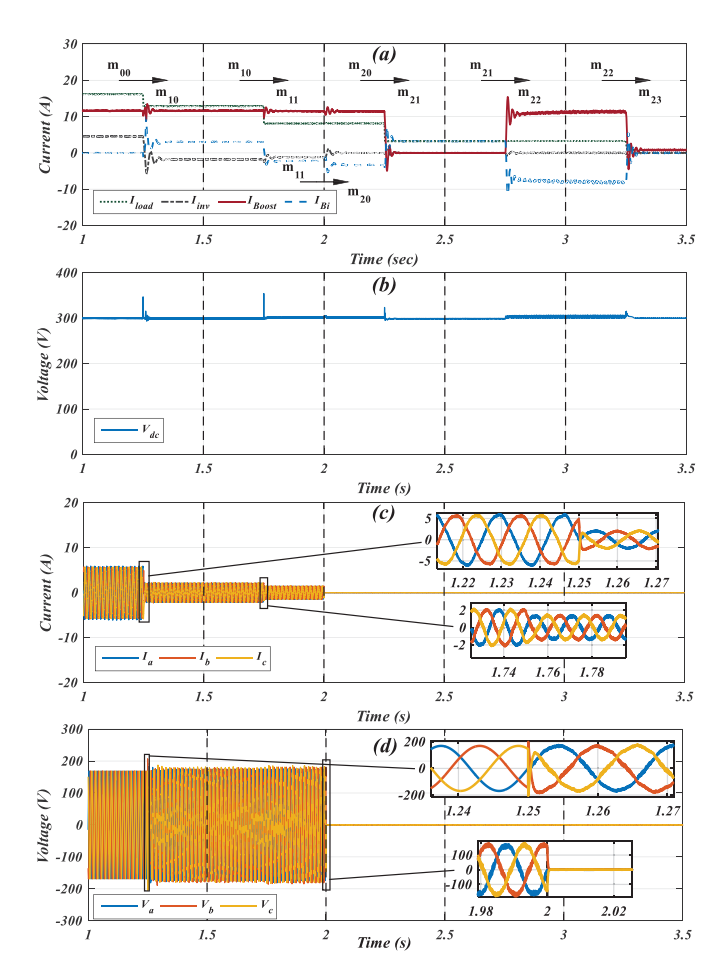


Fig. 13. Case IV shows the transition between grid-tied, islanding, and emergency modes.

voltage as shown in Fig. 13(a). The DC and AC load currents decreased due to load shedding execution as seen in Figs. 13(a) and 13(c). At the time 2 s, between segments (2) and (3), the SSR_{Inv} senses a fault and signals ($\mathcal{R}_{Inv}=1$), isolating the AC loads and the inverter from the DC MG.

This leads to a transition from m_{11} to m_{20} . The DC load stays the same, i.e., no reconnection, as can be seen in Fig. 13(a). The AC current dropped to zero, as shown in Fig. 13(c). Moreover, the DC current from the inverter to the AC load dropped to zero. The excess current is utilized for charging the battery system, since the bidirectional converter is regulating the DC bus voltage, which can be observed in Fig. 13(a). During segment (3), SSR_{Bo} signals the tripping of the boost converter ($\mathcal{R}_{Bo} = 1$), and since the last status of SSR_{Bi} was available ($\mathcal{R}_{Bi} = 0$), a transition from m₂₁ to m₂₂ occurs. Throughout m₂₂, the MGCC commands the LC_{Bi} to regulate the DC bus voltage, which can be seen in Fig. 13(a), where the boost converter output current drops to zero, and the DC load current coincides with the bidirectional converter output current. In segment (4), SSR_{Bo} signals that the fault has been cleared and the boost converter is ready to be reconnected ($\mathcal{R}_{Bo} = 0$). Once the boost converter was reconnected, no load reconnection happens, because of the downstream load shedding condition discussed earlier. The bidirectional converter takes the extra current to charge the battery system,

TABLE A.I
INDUCTANCES AND CAPACITANCE OF THE
CONVERTERS UTILIZED IN THE DC MG

Converter	Component	Value
	L_{BDI}	4.5 mH, 0.25 Ohms
Bidirectional	L_{BD2}	8 mH, 1 Ohms
converter	C_{BDI}	890 μF
	C_{BD2}	1200 μF
	L_{BI}	4.5 mH, 0.25 Ohms
Boost converter	L_{B2}	8 mH, 1 Ohms
Boost converter	C_{BI}	1200 μF
	C_{B2}	1200 μF
-	L_{DC}	19m H, 1.4 Ohms
Inverter	C_{DC}	1488 μF
	L_{AC}	3-phase each (19 mH, 1 Ohms)

maintaining the DC bus voltage to 300 V, which can be seen in Fig. 13(a). During the last segment, SSR_{Bi} signals the tripping of the bidirectional converter ($\mathcal{R}_{Bi}=0$), and the last status of the boost converter from segment (4) was available ($\mathcal{R}_{Bo}=0$), a transition from m_{22} to m_{23} takes place. Within m_{23} , the MGCC triggers the maximum level of DC load shedding, and the boost converter regulates the DC bus voltage. This can be observed in Fig. 13(a). The bidirectional converter output current drops to zero once tripped as shown in Fig. 13(a). The DC load current drops to (\sim 10-20% of $P_{pv}|_{Lst4}$) and becomes equal to the boost converter output current, which regulates the DC bus voltage as shown in Figs. 13(a) and 13(b).

VI. CONCLUSION

In this paper, a communication-based hierarchical heuristic hybrid state/event control scheme for DC microgrids was developed and verified. A mathematical model that is based on Finite State Machine was developed to realize the proposed control scheme, and analytically relate state variables and triggering events, during all conceived modes of operation. To reduce communication network requirement, a hierarchical hybrid design was adopted. Primary controllers are state driven and require continuous communication. This does not impose challenging communication requirements since primary controllers (or local controllers) are typically collocated with their corresponding converters. Secondary control is event driven; therefore, communication is only needed when a new event takes place.

Several cases were studied to examine the validity and applicability of the proposed control scheme with reduced communication load and computational cycles. Results show that the proposed scheme can preserve reliable/stable and resilient microgrid operation throughout various severe scenarios. Since DC microgrid stability is highly related to that of its DC bus voltage. During all possible scenarios and transition, the DC bus voltage was maintained constant while supplying the required loads. It was shown that the proposed state/event control scheme reduces the communication load

TABLE A.II Transitions Between Operational Sub-Modes Within the Grid-Tied/Energy Saving Mode

0: Off s	Event 0: Off state 1: On state		Transition		
E_P	R_{Bi}	SOC	Current Mode Next Mode		Transition Drive
1	0	1	En anov Savina	Charging	Energy price is low, bidirectional converter is available, and batteries are not fully charged
0	0	0	Energy Saving -	discharging	Energy price is high, bidirectional converter is available, and batteries are fully/near full charged
_	1	0	Chamina	Energy Saving	Bidirectional is tripped or batteries are fully charged
	-	-	Charging –	discharging	N/A
_	1	1	dianhanaina	Energy Saving	Bidirectional is tripped or batteries are not fully charged
_	-	-	discharging -	Charging	N/A

TABLE A.III Transitions Between Operational Modes Within the Core Mode

Events 0: Off state 1: On state					Transition				Transition drive
RGrid	Rinv	R_{Bo}	R_{Bi}	S_{DC}	S_{AC}	Ç U	Current Mode	Next Mode	transition drive
1	-	-	-	-	1	-		Islanded	Blackout or disturbance of utility AC power occurred
-	1	-	-	-	-	-	- Grid-Tie	Emergency	Inverter is tripped
0	0	0	0	-	-	1	Gild-Tie	Utility	Utility request control while all resources operational
1	1	1	1	-	-	-		Shut Down	Absence of all resources
0	-	-	-	-	0	-		Grid-Tie	Fault is cleared and resynchronization is ready
-	1	-	-	-	-	-	-	Emergency	Inverter is tripped
-	-	-	-	-	-	-	Islanded	Utility	N/A
1	1	1	1	0	0	-	-	Shut Down	Absence of all resources or AC/DC violations beyond permissible limits occurred
-	0	-	-	=	0	-		Grid-Tie	Inverter/AC-DC link is restored and reconnection condition is satisfied
-	0	-	-	-	-	-	- -	Islanded	Inverter/AC-DC link is restored
-	-	-	-	-	-	-	- Emergency	Utility	N/A
1	-	1	1	-	-	-	-	Shut Down	Absence of all resources or DC violations beyond permissible limits occurred
1	1	1	1	-	-	0		Grid-Tie	Utility stops controlling the DC MG or any of the resources/converters is tripped
1	-	-	-	-	1	-	Utility	Islanded	Blackout or disturbance of Utility AC power occurred
-	1	-	-	-	-	-	- ,	Emergency	Inverter is tripped
1	1	11	1	-	-		-	Shut Down	Absence of all resources
-	-	-	-	-	-	-		Grid-Tie	N/A
-	-	-	-	-	-	-	Class Dan	Islanded	N/A
-	-	-	-	-	-	-	- Shut Down	Emergency	N/A
-	-	-	-	-	-	-	-	Utility	N/A

TABLE A.IV Transitions Between Operational Sub-Modes Within the Emergency Mode

Event 0: Off state 1: On state					Tran	sition	
R_{Bo}	R_{Bi}	SOC	SDC	B_{od}	Current Mode	Next Mode	Transition Drive
0	-	1	-	_		Contingency	Batteries are depleted and boost converter is available
1	0	-	-	1	Emergency	Critical	(Boost converter is tripped and bidirectional converter is available) or (over discharge last beyond t _s)
-	1	-	-	-	_	Extreme	Bidirectional converter is tripped
-	-	-	-	_		Emergency	N/A
1	0	-	1	-	Contingency	Critical	(Boost converter is tripped and bidirectional converter is available) or (DC bus voltage deviation last beyond t _s)
-	0	-	-	_	_	Extreme	Bidirectional converter is tripped
-	-	_	-	-		Emergency	N/A
-	-	-	-	-	— Critical	Contingency	N/A
0	1	1	-	=	- Critical	Extreme	(Boost converter is tripped and bidirectional converter is available) or (batteries are depleted)
0	-	-	-	-		Emergency	Bidirectional converter is available
-	-	-	-	-	Extreme	Contingency	N/A
-	-	-	-	=		Critical	N/A

and computational processing, which may lead to increased potentially lead to near-optimal operation, and enhanced dependence on communication within modern microgrid controls. Consequently, the proposed control scheme can

power quality and protection system functionalities of the MG.

Event 0: Off state 1: On state						Transition					
R_{Bo}	R_{Bi}	SOC	S_{AC}	S_{DC}	B_{od}	Current Mode	Next Mode	Transition Drive			
0	-	1	-	-	-		Contingency	Batteries are depleted and boost converter is available			
1	0	-	-	-	1	Islanded	Critical	(Boost converter is tripped and bidirectional converted available) or (over discharge last beyond t _s)			
-	1	-	-	-	-	<u>-</u>	Extreme	Bidirectional converter is tripped			
-	-	-	-	-	-		Islanded	N/A			
1	0	-	1	1	-	Contingency	Critical	(Boost converter is tripped and bidirectional converter is available) or (DC/AC bus voltage deviation last beyond t _s			
-	1	-	-	-	-	-	Extreme	Bidirectional converter is tripped			
-	-	-	-	-	-		Islanded	N/A			
-	-	-	-	-	-	G ::: 1	Contingency	N/A			
0	1	1	-	-	-	Critical	Extreme	(Boost converter is tripped and bidirectional converter is available) or (batteries are depleted)			
0	-	-	-	-	-		Islanded	Bidirectional converter is available			
-	_	-	-	-	-	Extreme	Contingency	N/A			
-	-	-	-	-	-	-	Critical	N/A			

TABLE A.V
TRANSITIONS BETWEEN OPERATIONAL SUB-MODES WITHIN THE ISLANDING MODE

TABLE A.VI K_D and K_i of Various Control Technique Used in the DC MG

Converter	Control	Outer Loop		Inner Loop			
	technique			Charge		Discharge	
		K_p	K_i	K_p	K_i	K_p	K_i
Bidirectional	Current control	N/A	N/A	0.02	110	0.02	3
converter	Voltage control	3	1	0.002	10	0.02	3
		Outer Loop		I_d		I_q	
	Current control	N/A	N/A	192.1	97671	192.1	97671
Inverter	DC voltage control	0.1	10	192.1	97671	192.1	97671
	AC voltage control	0.15	1	N/A	N/A	N/A	N/A
Boost converter	Voltage control	0.02	100	N/A	N/A	N/A	N/A

APPENDIX

Tables A.II, A.III, A.IV, and A.V show a list of the operational modes/sub-modes, and the transitions between them. It should be noted that the shaded cells indicate that an "or" operator has been applied in the logic. Tables A.I and A.VI show the values of the inductors and capacitors of the DC microgrid converters and the values of the K_p and K_i used for their controllers.

The controllers were mainly tuned using the signal constraint tool from MATLAB/Simulink, along with some trial and error considering the gain and phase margins of the system.

REFERENCES

 M. S. Saleh, A. Althaibani, Y. Esa, Y. Mhandi, and A. A. Mohamed, "Impact of clustering microgrids on their stability and resilience during blackouts," in *Proc. Int. Conf. Smart Grid Clean Energy Technol.* (ICSGCE), Offenburg, Germany, 2015, pp. 195–200.

- [2] M. Saleh, Y. Esa, Y. Mhandi, W. Brandauer, and A. Mohamed, "Design and implementation of CCNY DC microgrid testbed," in *Proc. IEEE Ind. Appl. Soc. Annu. Meeting*, Portland, OR, USA, 2016, pp. 1–7.
- [3] H. Farhangi, "The path of the smart grid," IEEE Power Energy Mag., vol. 8, no. 1, pp. 18–28, Jan./Feb. 2010.
- [4] D. T. Ton and M. A. Smith, "The U.S. department of energy's microgrid initiative," *Electricity J.*, vol. 25, no. 8, pp. 84–94, 2012.
- [5] N. Hatziargyriou, Ed., Microgrids: Architectures and Control. New York, NY, USA: Wiley, 2013, pp. 4–70.
- [6] F. Shahnia, S. Bourbour, and A. Ghosh, "Coupling neighboring microgrids for overload management based on dynamic multicriteria decision-making," *IEEE Trans. Smart Grid*, vol. 8, no. 2, pp. 969–983, Mar. 2017.
- [7] C. Marnay et al., "Microgrid evolution roadmap," in Proc. Int. Symp. Smart Elect. Distrib. Syst. Technol. (EDST), Sep. 2015, pp. 139–144.
- [8] E. Hossain, E. Kabalci, R. Bayindir, and R. Perez, "Microgrid testbeds around the world: State of art," *Energy Convers. Manag.*, vol. 86, pp. 132–153, Oct. 2014.
- [9] Z. Liu, X. Xu, H. A. Abdelsalam, and E. Makram, "Power system harmonics study for unbalanced microgrid system with PV sources and nonlinear loads," *J. Power Energy Eng.*, vol. 3, no. 5, pp. 43–55, 2015.
- [10] S. Backhaus et al., "DC scoping study—Estimate of technical and economic benefit," Los Alamos Nat. Lab., Los Alamos, NM, USA, Rep. LA-UR-15 22097, Mar. 2015.
- [11] H. Jiayi, J. Chuanwen, and X. Rong, "A review on distributed energy resources and MicroGrid," *Renew. Sustain. Energy Rev.*, vol. 12, no. 9, pp. 2472–2483, Dec. 2008.
- [12] L. Xiong, W. Peng, and P. C. Loh, "A hybrid AC/DC microgrid and its coordination control," *IEEE Trans. Smart Grid*, vol. 2, no. 2, pp. 278–286, Jun. 2011.
- [13] X. E. Planas, J. Andreu, J. I. Gárate, I. M. de Alegría, and E. Ibarra, "AC and DC technology in microgrids: A review," *Renew. Sustain. Energy Rev.*, vol. 43, pp. 726–749, Mar. 2015.
- [14] E. Unamuno and J. A. Barrena, "Hybrid AC/DC microgrids—Part I: Review and classification of topologies," *Renew. Sustain. Energy Rev.*, vol. 52, pp. 1251–1259, Dec. 2015.
- [15] D. Chen and L. Xu, "Autonomous DC voltage control of a DC microgrid with multiple slack terminals," *IEEE Trans. Power Syst.*, vol. 27, no. 4, pp. 1897–1905, Nov. 2012.
- [16] R. S. Balog, "Autonomous local control in distributed DC power systems," Ph.D. dissertation, Dept. Elect. Comput. Eng., Univ. Illinois Urbana-Champaign, Champaign, IL, USA, 2006.
- [17] P. Karlsson and J. Svensson, "DC bus voltage control for a distributed power system," *IEEE Trans. Power Electron.*, vol. 18, no. 6, pp. 1405–1412, Nov. 2003.
- [18] F. Katiraei, M. R. Iravani, and P. W. Lehn, "Micro-grid autonomous operation during and subsequent to islanding process," *IEEE Trans. Power Del.*, vol. 20, no. 1, pp. 248–257, Jan. 2005.

- [19] P. Piagi and R. H. Lasseter, "Autonomous control of microgrids," in Proc. IEEE Power Eng. Soc. Gen. Meeting, Montreal, QC, Canada, Jun. 2006, p. 8.
- [20] B. K. Johnson, R. H. Lasseter, F. L. Alvarado, and R. Adapa, "Expandable multiterminal DC systems based on voltage droop," *IEEE Trans. Power Del.*, vol. 8, no. 4, pp. 1926–1932, Oct. 1993.
- [21] V. Nasirian, S. Moayedi, A. Davoudi, and F. L. Lewis, "Distributed cooperative control of DC Microgrids," *IEEE Trans. Power Electron.*, vol. 30, no. 4, pp. 2288–2303, Apr. 2015.
- [22] Y. Ito, Y. Zhongqing, and H. Akagi, "DC microgrid based distribution power generation system," in *Proc. IPEMC*, Xi an, China, Aug. 2004, pp. 1740–1745.
- [23] J. H. Lee, H. J. Kim, and B. M. Han, "Operation analysis of a communication-based DC micro-grid using a hardware simulator," *J. Power Electron.*, vol. 13, no. 2, pp. 313–321, Mar. 2013.
- [24] T. Dragičević, X. Lu, J. C. Vasquez, and J. M. Guerrero, "DC microgrids—Part I: A review of control strategies and stabilization techniques," *IEEE Trans. Power Electron.*, vol. 31, no. 7, pp. 4876–4891, Jul 2016
- [25] M. Saleh, Y. Esa, and A. Moahmed, "Impact of communication latency on the bus voltage of centrally controlled DC microgrid during islanding," *IEEE Trans. Sustain. Energy*, to be published.
- [26] M. Saleh, Y. Esa, and A. Moahmed, "Centralized control for DC microgrid using finite state machine," presented at the IEEE Innov. Smart Grid Technol. Conf. (ISGT), Washington, DC, USA, Apr. 2017, pp. 1–5.
- [27] W. P. M. H. Heemels, J. H. Sandee, and P. P. J. van den Bosch, "Analysis of event-driven controllers for linear systems," *Int. J. Control*, vol. 81, no. 4, pp. 571–590, 2008.
- [28] J. H. Sandee, W. P. M. H. Heemels, and P. P. J. van den Bosch, "Case studies in event-driven control," in *Proc. Int. Workshop Hybrid Syst. Comput. Control*, 2007, pp. 762–765.
- [29] D. Salomonsson, L. Soder, and A. Sannino, "An adaptive control system for a DC microgrid for data centers," *IEEE Trans. Ind. Appl.*, vol. 44, no. 6, pp. 1910–1917, Nov./Dec. 2008.
- [30] Y. Zhu, F. Zhuo, and L. Xiong, "Communication platform for energy management system in a master–slave control structure microgrid," in *Proc. IPEMC ECCE*, Harbin, China, 2012, pp. 141–145.
- [31] J. M. Guerrero, J. C. Vasquez, J. Matas, L. G. de Vicuna, and M. Castilla, "Hierarchical control of droop-controlled AC and DC microgrids—A general approach toward standardization," *IEEE Trans. Ind. Electron.*, vol. 58, no. 1, pp. 158–172, Jan. 2011.
- [32] T. Dragičević, J. M. Guerrero, J. C. Vasquez, and D. Škrlec, "Supervisory control of an adaptive-droop regulated DC microgrid with battery management capability," *IEEE Trans. Power Electron.*, vol. 29, no. 2, pp. 695–706, Feb. 2014.
- [33] G. Turner, J. P. Kelley, C. L. Storm, D. A. Wetz, and W.-J. Lee, "Design and active control of a microgrid testbed," *IEEE Trans. Smart Grid*, vol. 6, no. 1, pp. 73–81, Jan. 2015.
- [34] K. Sakurama and M. Miura, "Communication-based decentralized demand response for smart microgrids," *IEEE Trans. Ind. Electron.*, vol. 64, no. 6, pp. 5192–5202, Jun. 2017, doi: 10.1109/TIE.2016.2631133.
- [35] W. Liu et al., "Decentralized multi-agent system-based cooperative frequency control for autonomous microgrids with communication constraints," *IEEE Trans. Sustain. Energy*, vol. 5, no. 2, pp. 446–456, Apr. 2014.
- [36] X. Lu, J. M. Guerrero, K. Sun, and J. C. Vasquez, "An improved droop control method for DC microgrids based on low bandwidth communication with DC bus voltage restoration and enhanced current sharing accuracy," *IEEE Trans. Power Electron.*, vol. 29, no. 4, pp. 1800–1812, Apr. 2014.

- [37] D. Chen, L. Xu, and L. Yao, "DC voltage variation based autonomous control of DC microgrids," *IEEE Trans. Power Del.*, vol. 28, no. 2, pp. 637–648, Apr. 2013.
- [38] M. Saleh, Y. Esa, and A. Mohamed, "Hardware based testing of communication based control for DC microgrid," in *Proc. Int. Conf. Renew. Energy Res. Appl. (ICRERA)*, San Diego, CA, USA, 2017, pp. 1–5.
- [39] J.-C. Choi et al., "Voltage control scheme with distributed generation and grid connected converter in a DC microgrid," Energies, vol. 7, no. 10, pp. 6477–6491, 2014.
- [40] IEEE Standard for Interconnecting Distributed Resources With Electric Power Systems, IEEE Standard 1547-2003, Jun. 2003.



Mahmoud Saleh received the M.S. degree in electrical engineering from City Collage of New York, in 2013, where he is currently pursuing the Ph.D. degree with the Smart Grid Laboratory, Department of Electrical Engineering. His research interest includes enhancing grid resilience, microgrids design, control and optimization, and the interdependencies between power systems, and communication networks.



Yusef Esa received the B.S. degree in electrical engineering from the City Collage of New York in 2015, where he is currently pursuing the M.S. degree with the Smart Grid Laboratory. His research interests include microgrids design and control and optimal power flow.



Ahmed A. Mohamed (El-Tallawy) (GS'09–M'13–SM'17) is an Assistant Professor of electrical engineering, and the Founding Director of the Smart Grid Laboratory, City University of New York, City College. He is also with the Department of Electrical Engineering (on leave), Menia University, Menia, Egypt. His current research interests include critical infrastructure interdependencies, smart grid resiliency, and electric transportation.